ACS OMEGA

http://pubs.acs.org/journal/acsodf

Article

NiF_2 Nanorod Arrays for Supercapattery Applications

Nanasaheb M. Shinde, Pritamkumar V. Shinde, Je Moon Yun, Krishna Chaitanya Gunturu, Rajaram S. Mane,* Colm O'Dwyer,* and Kwang Ho Kim*

Cite This: *ACS Omega* 2020, 5, 9768−9774

Read Online

ACCESS | Metrics & More | Article Recommendations | Supporting Information

ABSTRACT: A electrode for energy storage cells is possible directly on Ni foam, using a simple reduction process to form NiF_2 nanorod arrays (NA). We demonstrate NiF_2@Ni NA for a symmetric electrochemical supercapattery electrode. With an areal specific capacitance of 51 F cm^{-2} at 0.25 mA cm^{-2} current density and 94% cycling stability, a NiF_2@Ni electrode can exhibit supercapattery behavior, a combination of supercapacitor and battery-like redox. The symmetric electrochemical supercapattery delivers 31 W h m^{-2} energy density and 797 W m^{-2} power density with 83% retention in a 1 M KOH electrolyte, constituting a step toward manufacturing a laboratory-scale energy storage device based on metal halides. Producing self-grown hierarchically porous nanostructured electrodes on three-dimensional metal foams by displacement reactions may be useful for other metal halides as electrodes for supercapacitors, supercapatteries, and lithium-ion batteries.

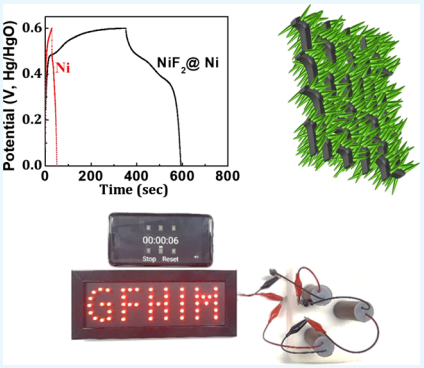

1. INTRODUCTION

Developing renewable energy sources such as solar, wind, wave, and geothermal energy in combination with energy storage devices that are affordable and cooperatively efficient is essential for a cleaner electricity-run society. Underlying the technological, industrial, and ecological importance is the ability to store and deliver energy in systems that use noncritical, abundant materials.[1,2] Sustainable materials developed for batteries, supercapacitors, electrochemical supercapatteries (supercapacitor + battery), and for other primary, secondary, and electrochemical charge storage (ECS) devices are important as the density of energy storage systems and infrastructure expands to power replacements to fossil-fuel burning transport, housing, industry, and other users.[3,4] If materials can be found to contribute to energy storage production technologies with higher efficiency and lower cost, that also work together synergistically, this would be immediately useful and important for fuel generation and energy storage applications.[5−7] The energy density (ED) and power density (PD), efficiency, specific capacitance (SC), rate capacity, and cycling stability of dual function electrode materials in ECS devices should be on par with existing materials, particularly with lower Co content materials now emerging.

Developing abundant, robust, scalable, and greener chemical routes for metal-oxides/hydroxides/carbides/nitrides/phosphides/layered double hydroxides etc., has seen some promising developments for both battery electrode materials.[8,9] We provide a comparison of recently published data on ECS application using $Ni(OH)_2$, NiO, Ni_xS_y, NiTe, NiSe, and so forth, electrodes, developed by simpler chemical reduction or electroless methods among others,[10−30] in Figure 1, with

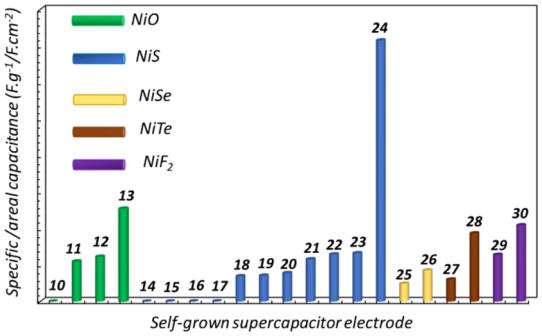

Figure 1. Comparison of specific/areal capacitances from previously published data in the literature. These comparisons relate relative performance as indicated by capacitances for supercapacitor/supercapattery systems of oxide/chalcogenide electrode materials grown by reduction, electroless deposition, or related methods on a suitable substrate material. The inset numbers correspond to relevant references.

further details on performance (capacitance) and related data provided in the Supporting Information, Table S1. Electrode materials grown by displacement, reduction, or electroless processes, for example, with high surface area and a strong mechanical adhesion to the underlying substrate material tend

Received: December 10, 2019
Accepted: February 20, 2020
Published: March 11, 2020

https://dx.doi.org/10.1021/acsomega.9b04219
ACS Omega 2020, 5, 9768−9774

to offer better performance than metal salt or binder inspired hydrothermally/chemically grown electrodes, although much of the improvement tends to be a geometrical enhancement, rather than an intrinsic one. This is in part because high surface areas expose several redox reactions,[31,32] and a better lattice match between the product and the base material promotes direct hopping-free charge/mass transport pathways with a minimum diffusion length and charge transfer resistance through a stronger interaction between the product material and the host.[33]

Rutile NiF_2 is a metal halide with antiferromagnetic properties, showing a weak ferromagnetic moment below the Néel point.[34] Few reports are available on NiF_2 as an ECS material with theoretical capacity 554 mA $h{\cdot}g^{-1}$,[35] and often where NiF_2 is grown by anodization of Ni-foil. In one study, the NiF_2 demonstrated SC 1280 F g^{-1} at 2 mV s^{-1}[29] In $Ni(OH)_2$−NiF_2 electrodes, the self-grown phase was $Ni(OH)_2$ and not NiF_2, which exhibited a SC of 2090 F g^{-1} at 10 mV s^{-1}[30] Noticeably, synthesis of NiF_2 in both reports was complicated and the final products were not phase pure, leading to less defined performance related to the NiF_2 phase. By comparison, for ECS systems, we are not aware of any reports using NiF_2.

Here, we report a metal salt and binder-free synthesis of NiF_2 nanorod-arrays (NA) on nickel-foam (NiF_2@Ni) as an electrode material by a simple reduction approach for ECS applications for the first time. A symmetric electrochemical symmetric supercapacitor (ESS) device fabricated with NiF_2@Ni//NiF_2@Ni configuration was capable of powering a light-emitting diode (LED) panel consisting of ∼60 LEDs with full-bright light intensity.

2. RESULTS AND DISCUSSION

The schematic summary of the hydrothermal growth of a NiF_2@Ni NA is shown in Figure 2a and the corresponding reaction mechanisms are detailed in the Supporting Information as Figure S1. Briefly, a reaction occurs between NiO and F during the hydrothermal process which facilitates the deposition of NiF_2 in NA morphology on Ni. In Figure 2b, the Ni surface changes from a polished finish (b1) to a rough texture with light green color after reaction (b2). The NiF_2@Ni NA adheres well to Ni and remained intact even after ultrasonication for 20 min. The field emission scanning electron microscopy (FE-SEM) surface images of three-dimensional 3D Ni-foam before and after NiF_2 growth are shown in Figure 2c1,c2−c4, respectively. Both Ni and F are uniformly distributed within each nanorod in the NiF_2@Ni NA in a 1:2 stoichiometric ratio, confirming surface conversion to NiF_2 (Figure 2c5,c6). The TEM images of individual nanorods of NiF_2, scratched from NiF_2@Ni are presented in Figure 2d. The growth is typically a single nanorod with broad-base and narrower tip. The nanorod of 88−263(±50) nm diameter and 500−1200(±200) nm length, is typical of the nanorod structure and forms a surface-bound array of tapered structures, confirmed under close inspection by FESEM. The high-resolution transmission electron microscopy (HR-TEM) image (Figure 2e) shows 0.331 and 0.221 nm interplanar distances between atomic columns of the [110] and [111] orientations within the NiF_2 structure.[29,30] The selected area electron diffraction (SAED) pattern evidenced stretched diffraction spots from a single crystal pattern, suggesting nanocrystalline NiF_2 in several relative orientations of the primary reflection axis (Figure 2f). The formation of NiF_2 on

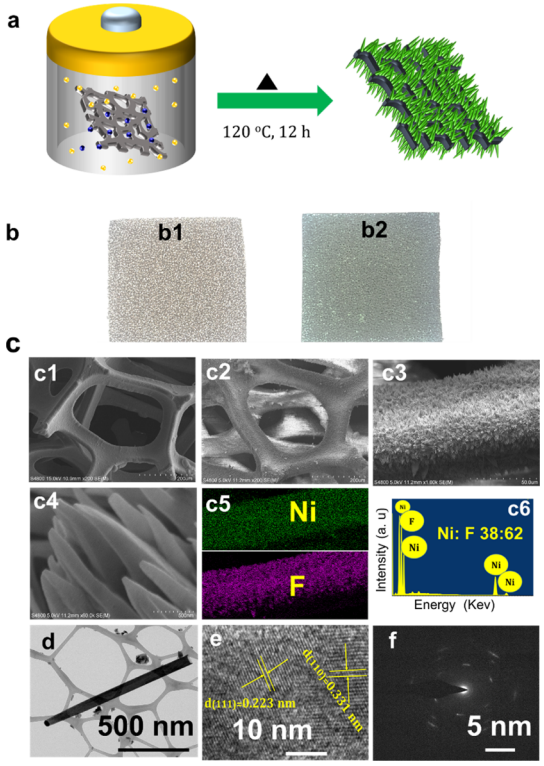

Figure 2. (a) Schematic representation of the deposition of the NiF_2@Ni NA coating using Ni-foam as the underlying electrode substrate. (b) Optical images of (b1) Ni-foam (left) and (b2) NiF_2@Ni NA (right). (c) FE-SEM images of Ni (c1) and (c2−c4) of NiF_2@Ni at different magnifications showing vertical NA growth onto the Ni-foam surface. EDS elemental mapping and corresponding spectrum (c5,c6) confirm a phase pure composition. (d−f) Bright field TEM, HR-TEM, and SAED of a single crystalline nanorod from the NiF_2@Ni NA coating.

Ni was confirmed by the X-ray diffraction (XRD) pattern shown in Figure 3a. Three welldefined reflections at 44.60, 51.97, and 76.59° (marked with "△") corresponding to the (111), (200), and (220) planes of the Ni (JCPDS no. 01-070-0989) were confirmed.[30] The (110), (101), (111), (210), (211), (220), (112), and (301) planes (marked with "black club suit") were of NiF_2 (JCPDS no. 01-074-2140),[29−39] confirming successful reaction to NiF_2 on Ni. Because of its metallic character, Ni has no clearly discernible Raman signature (Figure 3b), and oxides of Ni are not detected by Raman scattering here.[10] On the other hand, NiF_2@Ni exhibits two clear Raman bands caused by first-order optical LO phonon and the second-order two-phonon modes of NiF_2.[37]

The chemical valence states noted from the XPS spectrum for Ni and F in Figure 3c. On deconvoluting the Ni 2p core-level, two spin−orbit doublets and two shake-up satellites (abbreviated as "Sat.") peaks were identified (Figure 3d). The binding energies of 856.2 eV for Ni $2p_{3/2}$ and 876.3 eV for Ni $2p_{1/2}$ were spin−orbit characteristics of Ni 2p. The F 1s core-level emission exhibited a strong peak at 685.4 eV (Figure 3e).[11−13] As small chemical shift in the binding energy of Ni $2p_{3/2}$, Ni $2p_{1/2}$, and F 1s in the NiF_2@Ni NA compared with reported eigen-values is likely due to the transfer of electron density from the Ni and F due to the difference in their electro-negativity.[11] The nitrogen adsorption−desorption isotherm and corresponding pore-size distribution measurement, confirmed mesoporous and macro-porous structure, which we

https://dx.doi.org/10.1021/acsomega.9b04219
ACS Omega 2020, 5, 9768−9774

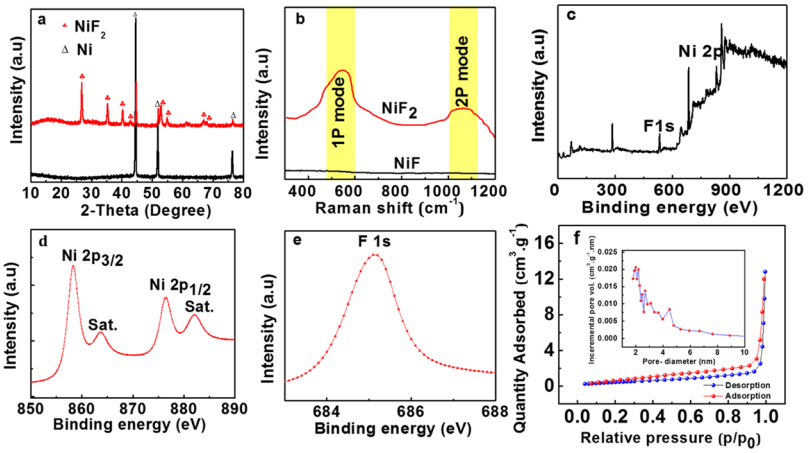

Figure 3. (a) XRD, and (b) Raman scattering spectra of NiF_2@Ni and the bare Ni-foam. (c–e) XPS survey spectrum and Ni 2p and F 1s core-level photoemission spectra. (f) N_2 adsorption isotherms of NiF_2@Ni NA presented following the BET model (pore-size distribution calculated using the BJH approach shown in the inset).

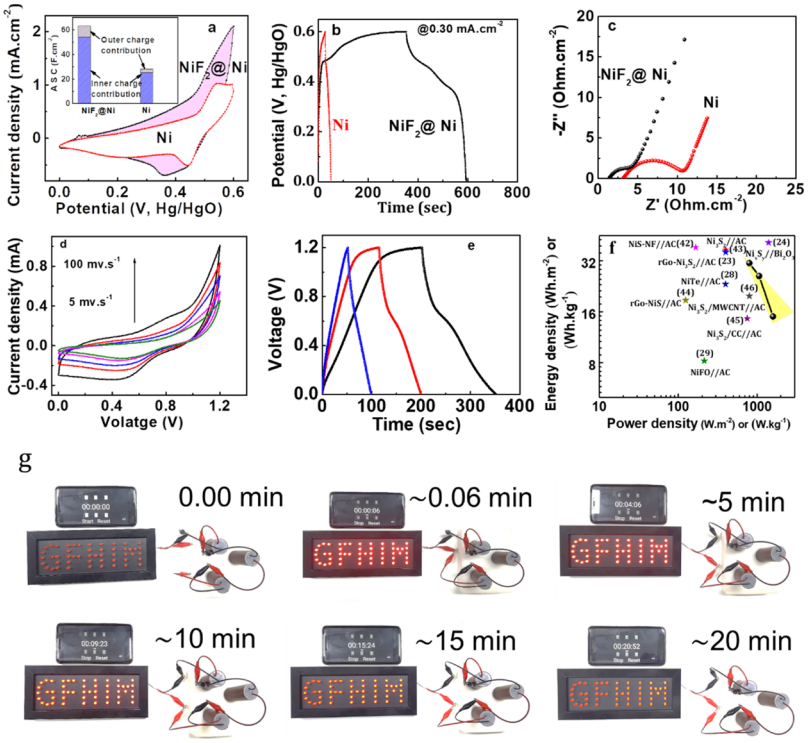

Figure 4. (a) CV of the Ni-foam compared to the NiF_2@Ni NA-coated Ni acquired at 25 mV s^{-1} scan rate. The inset shows the ratio of inner to outer charge contributions based on the ratio of faradaic to nonfaradaic processes. (b) GCD curves at 0.25 mA cm^{-2} current density, and (c) EIS of NiF_2@Ni NA and Ni electrodes. (d,e) CV at 5–25 mV s^{-1} and GCD at 0.30–0.60 mA cm^{-2} current density of the NiF_2@Ni//NiF_2@Ni ESS device. (f) The Ragone plot highlights the performance of the NiF_2-based ESS device compared to other materials and reports. (g) 60 LED panels fully lighted using three NiF_2@Ni//NiF_2@Ni ESS devices in series over 20 min time interval (photograph courtesy of "Nanasaheb M Shinde").

believe arises from the hierarchical pore sizes represented in the 0.6–0.9 and 0.9–1.0 P/P_0 ranges (Figure 3f).[24] The 25.10 m^2 g^{-1} specific area and 2.17 and 4.36 nm pore-diameters (see inset of Figure 3f) agree with the higher surface area and multiple porosity scales of NiF_2 NA on Ni (see Figure S2a of the Supporting Information for more details).

3. ELECTROCHEMICAL MEASUREMENTS

The three electrode-based electrochemical measurements of the NiF_2@Ni NA and Ni electrodes were evaluated using cyclic voltammetry (CV), galvanostatic charge–discharge (GCD), and electrochemical impedance spectroscopy (EIS) in a 1 M KOH aqueous electrolyte solution. The CV scans of NiF_2@Ni NA and Ni electrodes scanned in a 0.0–0.6 V potential range are shown in Figure 4a where we observe pseudocapacitive contributions from faradaic redox processes at the NiF_2@Ni NA surface. The possible reversible Faradaic reaction mechanism is suggested as follows[29,30]

$$NiF_2 + 2OH^- \leftarrow Ni(OH)_2 + HF \quad (1)$$

In Figure S2b,c, we present CV curves of Ni and NiF_2@Ni NA electrodes at 5–25 mV s^{-1} scan rates where we observe two separate regions, that is, a potential dependent current

https://dx.doi.org/10.1021/acsomega.9b04219
ACS Omega 2020, 5, 9768–9774

(capacitive), and current dependent (battery-type),[38,39] contributing to the total integrated charge. The contribution of the battery-type behavior (Figure S2b) dominates over capacitive kinetics in this new electrode. At higher scan rates, that is, ≥25 mV s^{-1} there was negligible change in the shape of CV curves. The shift in the anodic/cathodic peaks to lower and higher voltages, respectively, suggests quasi-Faradaic reversibility in this material, which we believe is caused by slow electron transfer kinetics and lower ionic conductivity.[40,41]

At 1, 5, 10, 15, and 25 mV s^{-1} scan rates, the areal specific capacitances (ASC) of the NiF_2@Ni NA were respectively 51, 13, 9, 7, and 5 F cm^{-2}, which is ascribed to a reduction in the migration speed of ions for redox reactions, as at higher scan rates and accessibility of inner active sites is limited.[11,12] Because of a high surface area and a mechanically robust adhesion with lowered interfacial resistance to the underlying Ni, the self-grown mesoporous NiF_2@Ni NA offers more accessible sites for redox reactions compared to polished Ni and similar nanostructured electrode materials of various composition and morphologies on Ni (see Table S1 of the Supporting Information).The inner/outer surface contributions to the ASC of NiF_2@Ni NA compared to Ni are shown in inset of Figure 4a, where we consistently observe a higher amount of charge (typically a factor of ∼2× greater) is stored on the NiF_2@Ni NA (for more details see the Supporting Information Figure S3a,b).[10−30] For both electrodes, at the initial potential of 0.2 V (vs Hg/HgO), the slope of 0.2 increased to 0.45 and reached 0.5 (indicating a diffusion-limited intercalative process) at potentials >0.4−0.5 V, indicating that NiF_2@Ni NA behaves as a battery-type material (see Figure S3c,d for more details).[40] Taken together, the intercalation capacitive contribution was more than 90% in both electrodes, signifying its dominance in the ASC performance (Figure S3e−h, Supporting Information) with higher values obtained for the NiF_2 nanorod coating. A comparison of GCD curves for Ni and NiF_2@Ni at 0.25−0.75 mA cm^{-2} confirms the higher ASC in NiF_2@Ni compared to Ni (see also Figures S3i,j of Supporting Information).

The NiF_2@Ni NA stores the charge using a capacitive mechanism in the potential range (0.1−0.4 V) whereas, the battery-type storage mechanism begins to dominate >0.4 V. The GCD measurements confirmed potential independency, as expected for a battery-type charge storage mechanism. The ASC values displayed in Figure S3k, were calculated from GCD curves (Figure 4b). For the NiF_2@Ni NA (49−25 F cm^{-2}) and Ni (16.00−0.90 F cm^{-2}) at current densities ranging from 0.25 to 0.75 mA cm^{-2}, the values were similar to integrated charge values obtained from the corresponding CV measurements. The NiF_2@Ni NA exhibited a higher ASC compared to Ni at 0.25 mA cm^{-2}, suggesting the NA electrode could provide a considerable an open space for electrolyte ions to access majority of electrode material (even at high current densities), resulting in three-fold increment in its ASC compared to Ni. A low equivalent series resistance (1.3 Ω) and charge transfer resistance (4.09 Ω) is found for the NiF_2@Ni compared to metallic Ni (6.45 Ω, Figure 4c) by electrochemical impedance suggests an improvement in the charge transport and redox reactions of NiF_2 over Ni.[30] The deviation in the vertical line at a low frequency region was accounted for the battery contribution.[39,40] In the low frequency region, there was no drastic change in both curves, suggesting negligible diffusion limitations.[27−30] A primary advantage of the NiF_2 phase, in addition to the accessible NA morphology, is the electrochemical stability. In strong base, Ni undergoes a complex but well-known oxidation process to hydroxides, oxyhydroxides ($Ni(OH)_2$, NiOOH), and oxides (NiO) which possess different electrical conductivity and surface redox chemistry. To confirm the cycling life, a representative stability of the NiF_2@Ni NA over 5000 operation cycles was conducted (Figure S3i) where the electrode achieved 90% ASC retention, an indication of better mechanical adhesion and considerable chemical stability. Inset of Figure S3i presents a FE-SEM image and EIS spectrum measured after an electrochemical stability test. The FE-SEM image has confirmed that the NiF_2 NAs type appearance has been destroyed into a clamped and stacked type because of the electrolyte ions adsorption/de-adsorption process. Whereas, in EIS spectrum, semicircle at the high frequency region after cycling, totally disappears, demonstrating relatively low charge transfer resistance, that is, an outstanding stability during cycling. To evaluate the performance of this state-of-the-art NiF_2@Ni//NiF_2@Ni (see device fabrication information in the Supporting Information and Figure S4) CV and GCD data are displayed in Figure 4d,e, respectively. Capacitive-type behavior was confirmed as the GCD discharge plots were free from the voltage plateau. The electrochemical symmetric supercapattery device with 3.25 cm^2 area supplied 15.84, 13.29, and 7.9 F cm^{-2} ASC at 0.3, 0.4, and 0.6 mA cm^{-2} current density, respectively. These NiF_2@Ni//NiF_2@Ni ESS cells output 31 W h m^{-2} ED or 797 W m^{-2} PD (Figure 4f). This new electrode performs very well against recently reported systems using similar growth methods, such as rGo-Ni_3S_2//AC (399 W kg^{-1}; 37.19 W h kg^{-1}),[23] Ni_xS_y//Bi_2O_3 (1399 W kg^{-1}; 41 W h kg^{-1}),[24] NiTe//AC (398.1 W h kg^{-1}; 23.341 W kg^{-1}),[28] NiFO//AC (214 W h kg^{-1}; 8.2 W kg^{-1}),[29] NiS-NF//AC (166.6 W h kg^{-1}; 38.4 W kg^{-1}),[42] Ni_3S_2//AC (400 W h kg^{-1}; 36 W kg^{-1}),[43] rGo-NiS//AC (124 W h kg^{-1}; 18.7 W kg^{-1}),[44] Ni_3S_2/CC//AC (750.8 W h kg^{-1}; 14.6 W kg^{-1}),[45] and Ni_3S_2/MWCNT//AC (798; 19.8 W h kg^{-1}).[46]

Our NiF_2-based ESS device electrodes are promising candidates for application as the positive electrode in high-performance energy storage systems. The durability of the NiF_2@Ni//NiF_2@Ni NA cell, tested over 5000 cycles at 5 mA cm^{-2} demonstrated ∼85% retention (Figure S5), confirming its chemical stability and mechanical robustness. Using three NiF_2@Ni//NiF_2@Ni ESS in series, whose electrochemical CV and GCD curves with series of combinations are displayed in Figure S6, where a basic law of series combination is obeyed with illumination of a color LED panel of our institute name comprising five letters, that is, "GFHIM", was built containing about 60 light-emitting diodes and operated with a full-bright light intensity (Figure 4g), suggesting a practical potential and industrial viability of self-grown NiF_2@Ni NA electrodes.

4. CONCLUSIONS

Deposition of polycrystalline and mesoporous NiF_2@Ni NA as an electrode coating for Ni with good mechanical adhesion is shown for the first time and demonstrated as an effective electrode material for electrochemical supercapattery in an aqueous electrolyte. A symmetric supercapattery device using NiF_2@Ni NA exhibits 51 F cm^{-2} ASC at 0.25 mA cm^{-2} current density and 94% cycling stability. The symmetric supercapattery system, with three-cells in series, possesses 31 W h m^{-2} ED and 797 W m^{-2} PD, which powered a display panel of ∼60 different colored LEDs with full intensity. For the

https://dx.doi.org/10.1021/acsomega.9b04219
ACS Omega 2020, 5, 9768−9774

geometrically activated improvement electrode for supercapacitor applications, for example, we acknowledge that electrodeposition approaches may also provide electrically interfaced, mechanically stable materials of phases that do not undergo displacement reactions with substrates, but these often require salt-containing electrolytes. Nevertheless, wetting of all available surface area is critical for the growth and electrochemical application, and so the nature of the underlying current collector and the grown material's porosity is important.

5. EXPERIMENTAL PROCEDURE

5.1. Synthesis Method. All chemical reagents such ethanol (C_2H_6O, 99%) and hydrofluoric acid (HF, 48%) and so forth, were purchased from the Sigma-Aldrich and were used as received. The Ni in 10 mm × 50 mm × 0.1 mm, 110 ppi (pores per inch) and mass density of 320 g m^{-2} was purchased from the Artenano Company Limited, Hong Kong. The NiF_2@Ni NA was self-grown on a piece of Ni via a one-step simple hydrothermal process. In a typical experiment, a cleaned Ni was transferred into a Teflon-lined stainless steel autoclave filled with 50 mL of ethanol water. A quantity of 2−4 mL of HF made up to 50 mL in ethanol was provided through microsyringe and autoclave was sealed well. The sealed autoclave was kept in an electric oven at 120 °C for 12 h to form NiF_2@Ni NA. Once the autoclave was cooled to room temperature (27 °C), the NiF_2@Ni NA electrode was removed, washed with distilled water and then dried at 60 °C under vacuum for 12 h before further measurements.

5.2. Physicochemical Measurements. Structural elucidation and morphological evolution studies of Ni and NiF_2@Ni were carried out using XRD (D8-Discovery Bruker, 40 kV, 40 mA, Cu Kα, λ = 1.5406 Å) in the θ−2θ geometry. Field-emission scanning electron microscopy was conducted using a FE-SEM, Hitachi, S-4800, at 15 kV accelerating voltage equipped with energy dispersive X-ray spectroscopy for the chemical composition analysis. Transmission and HR-TEM were carried out using a JEOL 2100F at 200 kV. Raman spectrophotometry measurements were performed on the Ni and NiF_2@Ni surfaces using a Raman spectrometer (Xper Ram 200, NanoBase, Korea) equipped with a 532 nm excitation laser source at 2.0 mW. X-ray photoelectron spectroscopy (XPS, VG Scientific ESCALAB250) measurement was carried out to analyze the chemical bonding status of the NiF_2@Ni. The X-ray measurement was operated at 1 × 10^{-9} mbar after inserting the sample into the analysis chamber at a base pressure of 2 to 4 × 10^{-8} mbar. The X-ray beam diameter was 500 μm and survey spectra of Ni and NiF_2@Ni were recorded with a pass energy of 150 eV and step size 1 eV with a dwell time of 50 ms. High-energy resolution spectra for Ni and F were recorded with 20 eV pass energy, 0.07 eV step size and 100 ms dwell time. Automated height adjustment to the highest intensity along the Z-direction was performed before each measurement to find the analyzer's focal point and the number of average sweeps of each of the elements was adjusted to obtain the optimal signal-to-noise ratio. Nitrogen adsorption/desorption isotherm spectra used to investigate the Brunauer, Emmett, and Teller (BET) surface area and Barrett−Joyner−Halenda pore-size distribution of NiF_2@Ni were conducted using a Micromeritics ASAP2010 analyzer.

5.3. Electrochemical Measurements. CV curves, GCD tests and EIS were carried out using the IVIUM electrochemical workstation system (Ivium, State). All electrochemical measurements were carried out in a conventional three-electrode system, that is, the Ni/NiF_2@Ni-working electrode, the Hg/HgO-reference electrode, and the Pt-reference electrode, with a 0.1 M KOH aqueous electrolyte at room temperature. The NiF_2@Ni//NiF_2@Ni SC device was fabricated using a sheet of separator in a plastic cell and two wires from both electrodes were carefully drawn before sealing the pencil plastic cell for electrical processing. The ASC, balance equation, ED and PD, can be calculated from the discharge profile using the relationships given below

$$C = \frac{I\Delta t}{A\Delta V} \tag{2}$$

where I is the discharge current, Δt is discharge time, A is the area of the active (1 × 1 cm^2 with its 3.8 mg mass) material, and ΔV is the potential window.

The NiF_2@Ni//NiF_2@Ni device ED and PD are calculated as

$$\mathrm{ED} = \frac{1}{2}C\Delta V^2 \tag{3}$$

$$\mathrm{PD} = \frac{E}{\Delta t} \times 3600 \tag{4}$$

In this calculation formula, C is the ASC of the for NiF_2@Ni//NiF_2@Ni device, ΔV is the potential window (V), and Δt is the discharging time.

■ ASSOCIATED CONTENT

Supporting Information

The Supporting Information is available free of charge at https://pubs.acs.org/doi/10.1021/acsomega.9b04219.

Comparative table of electrochemical analysis; reaction mechanism; BET, CV, GCD, and Trasatti plots; and stability and device fabrication (PDF)

■ AUTHOR INFORMATION

Corresponding Authors

Rajaram S. Mane − *School of Physical Sciences, Swami Ramanand Teerth Marathwada University, Nanded 431606, India;* orcid.org/0000-0002-9624-7985; Email: rajarammane70@srtmun.acin

Colm O'Dwyer − *School of Chemistry and Environmental Research Institute, University College Cork, Cork T12 YN60, Ireland; Micro-Nano Systems Centre, Tyndall National Institute, Cork T12 R5CP, Ireland; AMBER@CRANN, Trinity College Dublin, Dublin 2, Ireland;* orcid.org/0000-0001-7429-015X; Email: c.odwyer@ucc.ie

Kwang Ho Kim − *National Core Research Centre for Hybrid Materials Solution, Global Frontier R&D Center for Hybrid Interface Materials, and School of Materials Science and Engineering, Pusan National University, Busan 609-735, Republic of Korea*; Email: kwhokim@pusan.ac.kr

Authors

Nanasaheb M. Shinde − *National Core Research Centre for Hybrid Materials Solution, Pusan National University, Busan 609-735, Republic of Korea*

Pritamkumar V. Shinde − *Global Frontier R&D Center for Hybrid Interface Materials, Pusan National University, Busan 609-735, Republic of Korea;* orcid.org/0000-0002-2061-6852

https://dx.doi.org/10.1021/acsomega.9b04219
ACS Omega 2020, 5, 9768−9774

Je Moon Yun − *Global Frontier R&D Center for Hybrid Interface Materials, Pusan National University, Busan 609-735, Republic of Korea;* orcid.org/0000-0001-6565-6375

Krishna Chaitanya Gunturu − *School of Chemical Sciences, Swami Ramanand Teerth Marathwada University, Nanded 431606, India*

Complete contact information is available at: https://pubs.acs.org/10.1021/acsomega.9b04219

Notes

The authors declare no competing financial interest.

■ ACKNOWLEDGMENTS

This study was supported by The Global Frontier Program through the Global Frontier Hybrid Interface Materials (GFHIM) of the National Research Foundation of Korea (NRF) funded by the Ministry of Science, ICT & Future Planning (2013 M3A6B1078874), the National Core Research Centre (NCRC) grant 2015M3A6B1065262. This publication has also emanated from research supported in part by a research grant from SFI under grant no. 14/IA/2581. Authors are indebted to Seonghee Jeong, Sr. for FE-SEM analyses.

■ REFERENCES

(1) Ellabban, O.; Abu-Rub, H.; Blaabjerg, F. Renewable energy resources: Current Status, Future Prospects and Their Enabling Technology. *Renewable Sustainable Energy Rev.* **2014**, *39*, 748−764.

(2) Conway, B. E. *Electrochemical Supercapacitors: Scientific Fundamentals and Technological Applications*; Springer Science & Business Media, 2013.

(3) Simon, P.; Gogotsi, Y.; Dunn, B. Where do Batteries End and Supercapacitors Begin? *Science* **2014**, *343*, 1210−1211.

(4) Brousse, T.; Bélanger, D.; Long, J. W. To Be or Not To Be pseudocapacitive? *J. Electrochem. Soc.* **2015**, *162*, A5185−A5189.

(5) Sun, M.-H.; Huang, S.-Z.; Chen, L.-H.; Li, Y.; Yang, X.-Y.; Yuan, Z.-Y.; Su, B.-L. Applications of Hierarchically Structured Porous Materials from Energy Storage and Conversion, Catalysis, Photocatalysis, Adsorption, Separation, and Sensing to Biomedicine. *Chem. Soc. Rev.* **2016**, *45*, 3479−3563.

(6) Jiang, J.; Sun, F.; Zhou, S.; Hu, W.; Zhang, H.; Dong, J.; Jiang, Z.; Zhao, J.; Li, J.; Yan, W.; Wang, M. Atomic-level Insight into Super-efficient Electrocatalytic Oxygen Evolution on Iron and Vanadium Co-doped nickel (oxy) Hydroxide. *Nat. Commun.* **2018**, *9*, 2885.

(7) Han, N.; Liu, P.; Jiang, J.; Ai, L.; Shao, Z.; Liu, S. Recent Advances in Nanostructured Metal Nitrides for Water Splitting. *J. Mater. Chem. A* **2018**, *6*, 19912−19933.

(8) Ko, Y.; Kwon, M.; Bae, W. K.; Lee, B.; Lee, S. W.; Cho, J. Flexible Supercapacitor Electrodes Based on Real Metal-like Cellulose Papers. *Nat. Commun.* **2017**, *8*, 536.

(9) Tyagi, A.; Tripathi, K. M.; Gupta, R. K. Recent Progress in Micro-scale Energy Storage Devices and Future Aspects. *J. Mater. Chem. A* **2015**, *3*, 22507−22541.

(10) Yu, M.; Wang, W.; Li, C.; Zhai, T.; Lu, X.; Tong, Y. Scalable Self-growth of Ni@ NiO Core-shell Electrode with Ultrahigh Capacitance and Super-long Cyclic Stability for Supercapacitors. *NPG Asia Mater.* **2014**, *6*, No. e129.

(11) Xu, J. M.; Ma, K. Y.; Cheng, J. P. Controllable in Situ Synthesis of $Ni(OH)_2$ and NiO Films on Nickel foam as Additive-free Electrodes for Electrochemical capacitors. *J. Alloys Compd.* **2015**, *653*, 88−94.

(12) Hu, B.; Qin, X.; Asiri, A. M.; Alamry, K. A.; Al-Youbi, A. O.; Sun, X. Fabrication of $Ni(OH)_2$ Nanoflakes Array on Ni foam as a Binder-free Electrode Material for High Performance Supercapacitors. *Electrochim. Acta* **2013**, *107*, 339−342.

(13) Li, L.; Xu, J.; Lei, J.; Zhang, J.; McLarnon, F.; Wei, Z.; Li, N.; Pan, F. A One-step, Cost-effective Green Method to in Situ Fabricate $Ni(OH)_2$ Hexagonal Platelets on Ni foam as Binder-free Supercapacitor EelectrodeMaterials. *J. Mater. Chem. A* **2015**, *3*, 1953−1960.

(14) Zhuo, M.; Zhang, P.; Chen, Y.; Li, Q. Facile Construction of Graphene-like Ni_3S_2 Nanosheets Through the Hydrothermally Assisted Sulfurization of Nickel foam and Their Application as Self-supported Electrodes for Supercapacitors. *RSC Adv.* **2015**, *5*, 25446−25449.

(15) Li, J.; Wang, S.; Xiao, T.; Tan, X.; Xiang, P.; Jiang, L.; Deng, C.; Li, W.; Li, M. Controllable Preparation of Nanoporous Ni_3S_2 films by Sulfuration of nickel Foam as Promising Asymmetric Supercapacitor Electrodes. *Appl. Surf. Sci.* **2017**, *420*, 919−926.

(16) Li, X.-X.; Chen, G.-F.; Xiao, K.; Li, N.; Ma, T.-Y.; Liu, Z.-Q. Self-supported amorphous-edge nickel Sulfide Nanobrush for Excellent Energy Storage. *Electrochim. Acta* **2017**, *255*, 153−159.

(17) Yilmaz, G.; Lu, X. Direct Growth of 3D Hierarchical Porous Ni_3S_2 Nanostructures on Nickel Foam for High-Performance Supercapacitors. *ChemNanoMat* **2016**, *2*, 719−725.

(18) Xiong, X.; Zhao, B.; Ding, D.; Chen, D.; Yang, C.; Lei, Y.; Liu, M. One-step Synthesis of Architectural Ni_3S_2 Nanosheet-on-nanorods Array for Use as High-Performance Electrodes for Supercapacitors. *NPG Asia Mater.* **2016**, *8*, No. e300.

(19) Zhang, Z.; Huang, Z.; Ren, L.; Shen, Y.; Qi, X.; Zhong, J. One-pot Synthesis of Hierarchically Nanostructured Ni_3S_2 Dendrites as Active Materials for Supercapacitors. *Electrochim. Acta* **2014**, *149*, 316−323.

(20) Yang, J.; Guo, W.; Li, D.; Wei, C.; Fan, H.; Wu, L.; Zheng, W. Synthesis and Electrochemical Performances of Novel Hierarchical Flower-like Nickel Sulfide with Tunable Number of Composed Nanoplates. *J. Power Sources* **2014**, *268*, 113−120.

(21) Li, W.; Wang, S.; Xin, L.; Wu, M.; Lou, X. Single-Crystal β-NiS Nanorod Arrays with a Hollow-Structured Ni_3S_2 Framework for Supercapacitor Applications. *J. Mater. Chem. A* **2016**, *4*, 7700−7709.

(22) Krishnamoorthy, K.; Veerasubramani, G. K.; Radhakrishnan, S.; Kim, S. J. One Pot Hydrothermal Growth of Hierarchical Nanostructured Ni_3S_2 on Ni foam for Supercapacitor Application. *Chem. Eng. J.* **2014**, *251*, 116−122.

(23) Lin, H.; Liu, F.; Wang, X.; Ai, Y.; Yao, Z.; Chu, L.; Han, S.; Zhuang, X. Graphene-Coupled Fower-like Ni_3S_2 for a Free-standing 3D Aerogel with an Ultra-high Electrochemical Capacity. *Electrochim. Acta* **2016**, *191*, 705−715.

(24) Shinde, N. M.; Xia, Q. X.; Shinde, P. V.; Yun, J. M.; Mane, R. S.; Kim, K. H. Sulphur Source-Inspired Self-Grown 3D Ni_xS_y Nanostructures and Their Electrochemical Supercapacitors. *ACS Appl. Mater. Interfaces* **2019**, *11*, 4551−4559.

(25) Guo, K.; Yang, F.; Cui, S.; Chen, W.; Mi, L. Controlled Synthesis of 3D Hierarchical NiSe Microspheres for High-performance Supercapacitor Design. *RSC Adv.* **2016**, *6*, 46523−46530.

(26) Jiang, S.; Wu, J.; Ye, B.; Fan, Y.; Ge, J.; Guo, Q.; Huang, M. Growth of Ni_3Se_2 nanosheets on Ni foam for Asymmetric Supercapacitors. *J. Mater. Sci. Mater. Electron.* **2018**, *29*, 4649−4657.

(27) Ye, B.; Huang, M.; Bao, Q.; Jiang, S.; Ge, J.; Zhao, H.; Fan, L.; Lin, J.; Wu, J. Construction of NiTe/NiSe Composites on Ni Foam for High-Performance Asymmetric Supercapacitor. *ChemElectroChem* **2018**, *5*, 507−514.

(28) Ye, B.; Huang, M.; Jiang, S.; Fan, L.; Lin, J.; Wu, J. In-situ Growth of Se-doped NiTe on nickel foam as Positive Electrode Material for High-performance Asymmetric Supercapacitor. *Mater. Chem. Phys.* **2018**, *211*, 389−398.

(29) Yang, Y.; Li, L.; Ruan, G.; Fei, H.; Xiang, C.; Fan, X.; Tour, J. M. Hydrothermally Formed Three-dimensional Nanoporous $Ni(OH)_2$ Thin-film Supercapacitors. *ACS Nano* **2014**, *8*, 9622−9628.

(30) Jin, M.; Zhang, G.; Yu, F.; Li, W.; Lu, W.; Huang, H. Sponge-like $Ni(OH)_2$−NiF_2Composite Film with Excellent Electrochemical Performance. *Phys. Chem. Chem. Phys.* **2013**, *15*, 1601−1605.

(31) Chen, G. Z. Understanding Supercapacitors Based on Nano-hybrid Materials with Interfacial Conjugation. *Prog. Nat. Sci.: Mater. Int.* **2013**, *23*, 245−255.

(32) Jin, H.; Wang, J.; Su, D.; Wei, Z.; Pang, Z.; Wang, Y. In Situ Cobalt−cobalt oxide/N-doped Carbon Hybrids as Superior Bifunc-

tional Electrocatalysts for Hydrogen and Oxygen Evolution. *J. Am. Chem. Soc.* **2015**, *137*, 2688−2694.
(33) Tian, J.; Liu, Q.; Asiri, A. M.; Sun, X. Self-supported Nanoporous Cobalt Phosphide Nanowire Arrays: an Efficient 3D Hydrogen-evolving Cathode Over the Wide Range of pH 0−14. *J. Am. Chem. Soc.* **2014**, *136*, 7587−7590.
(34) Zou, G.; Shi, W.; Xiang, S.; Ji, X.; Ma, G.; Ballinger, R. G. Corrosion Behavior of 904L Austenitic Stainless Steel in Hydrofluoric Acid. *RSC Adv.* **2018**, *8*, 2811−2817.
(35) Karuppiah, J.; Linga Reddy, E.; Sudhakaran, M. S. P.; Lee, S. B. Production of Synthesis Gas from Dry Reforming of Propane with Carbon dioxide Over Ceria-promoted nickel foam Catalysts. *Renew. Energy Power Qual.* **2016**, *1*, 742−747.
(36) Seo, J. K.; Cho, H.-M.; Takahara, K.; Chapman, K. W.; Borkiewicz, O. J.; Sina, M.; Shirley Meng, Y. Revisiting the Conversion Reaction Voltage and the Reversibility of the CuF_2 electrode in Li-ion Batteries. *Nano Res.* **2017**, *10*, 4232−4244.
(37) Ding, R.; Li, X.; Shi, W.; Xu, Q.; Wang, L.; Jiang, H.; Yang, Z.; Liu, E. Mesoporous Ni-P Nanocatalysts for Alkaline Urea Electro-oxidation. *Electrochim. Acta* **2016**, *222*, 455−462.
(38) Sankar, K. V.; Seo, Y.; Lee, S. C.; Liu, S.; Kundu, A.; Ray, C.; Jun, S. C. Cobalt Carbonate Hydroxides as Advanced Battery-type Materials for Supercapatteries: Influence of Morphology on Performance. *Electrochim. Acta* **2018**, *259*, 1037−1044.
(39) Biesinger, M. C.; Lau, L. W. M.; Gerson, A. R.; Smart, R. S. C. The Role of the Auger parameter in XPS Studies of Nickel Metal, Halides and Oxides. *Phys. Chem. Chem. Phys.* **2012**, *14*, 2434−2442.
(40) Kim, H.-S.; Cook, J. B.; Lin, H.; Ko, J. S.; Tolbert, S. H.; Ozolins, V.; Dunn, B. Oxygen Vacancies Enhance Pseudocapacitive Charge Storage Properties of MoO_{3-x}. *Nat. Mater.* **2017**, *16*, 454−460.
(41) Li, W.; Wang, S.; Xin, L.; Wu, M.; Lou, X. Single-crystal β-NiS Nanorod Arrays with a Hollow-structured Ni_3S_2 Framework for Supercapacitor Applications. *J. Mater. Chem. A* **2016**, *4*, 7700−7709.
(42) Yu, L.; Yang, B.; Liu, Q.; Liu, J.; Wang, X.; Song, D.; Wang, J.; Jing, X. Interconnected NiS Nanosheets Supported by nickel foam: Soaking Fabrication and Supercapacitors Application. *J. Electroanal. Chem.* **2015**, *739*, 156−163.
(43) Li, J.-J.; Hu, Y. X.; Liu, M. C.; Kong, L. B.; Hu, Y. M.; Han, W.; Luo, Y. C.; Kang, L. Mechanical Alloying Synthesis of Ni_3S_2 Nanoparticles as Electrode Material for Pseudocapacitor with Excellent Performances. *J. Alloys Compd.* **2016**, *656*, 138−145.
(44) Cai, F.; Sun, R.; Kang, Y.; Chen, H.; Chen, M.; Li, Q. One-step Strategy to a Three-dimensional NiS-reduced Graphene Oxide Hybrid Nanostructure for High Performance Supercapacitors. *RSC Adv.* **2015**, *5*, 23073−23079.
(45) Huang, F.; Sui, Y.; Wei, F.; Qi, J.; Meng, Q.; He, Y. Ni_3S_4Supported on Carbon Cloth for High-performance Flexible All-solid-state Asymmetric Supercapacitors. *J. Mater. Sci.: Mater. Electron.* **2018**, *29*, 2525−2536.
(46) Dai, C.-S.; Chien, P.-Y.; Lin, J.-Y.; Chou, S.-W.; Wu, W.-K.; Li, P.-H.; Wu, K.-Y.; Lin, T.-W. Hierarchically Structured Ni_3S_2/carbon Nanotube Composites as High Performance Cathode Materials for Asymmetric Supercapacitors. *ACS Appl. Mater. Interfaces* **2013**, *5*, 12168−12174.

https://dx.doi.org/10.1021/acsomega.9b04219
ACS Omega 2020, 5, 9768−9774